Geophys. J. Int. (2011) **186,** 1285–1294 doi: 10.1111/j.1365-246X.2011.05106.x

2.5-D poroelastic wave modelling in double porosity media

Xu Liu,[1,2] Stewart Greenhalgh[2,3] and Yanghua Wang[1]

[1] *Centre for Reservoir Geophysics, Imperial College London, UK. E-mail: xu.liu@imperial.ac.uk*
[2] *Department of Physics, University of Adelaide, Australia*
[3] *Institute of Geophysics, ETH Zürich, Switzerland*

Accepted 2011 June 5. Received 2011 May 31; in original form 2010 June 2

SUMMARY

To approximate seismic wave propagation in double porosity media, the 2.5-D governing equations of poroelastic waves are developed and numerically solved. The equations are obtained by taking a Fourier transform in the strike or medium-invariant direction over all of the field quantities in the 3-D governing equations. The new memory variables from the Zener model are suggested as a way to represent the sum of the convolution integrals for both the solid particle velocity and the macroscopic fluid flux in the governing equations. By application of the memory equations, the field quantities at every time step need not be stored. However, this approximation allows just two Zener relaxation times to represent the very complex double porosity and dual permeability attenuation mechanism, and thus reduce the difficulty. The 2.5-D governing equations are numerically solved by a time-splitting method for the non-stiff parts and an explicit fourth-order Runge-Kutta method for the time integration and a Fourier pseudospectral staggered-grid for handling the spatial derivative terms. The 2.5-D solution has the advantage of producing a 3-D wavefield (point source) for a 2-D model but is much more computationally efficient than the full 3-D solution. As an illustrative example, we firstly show the computed 2.5-D wavefields in a homogeneous single porosity model for which we reformulated an analytic solution. Results for a two-layer, water-saturated double porosity model and a laterally heterogeneous double porosity structure are also presented.

Key words: Numerical solutions; elasticity and anelasticity; seismic attenuation; wave propagation.

1 INTRODUCTION

By applying a volume averaging theory to the local Biot poroelastic law, Pride & Berryman (2003a,b) developed the double-porosity, dual permeability (DPDP) model. It provides a theoretical framework to model acoustic (not elastic) wave propagation through heterogeneous porous structures. All of the field quantities, such as confining pressure and solid phase particle velocity, are actually the averaged values over a representative volume of mesoscopic size including the two fluid-filled porous constituents, phase 1 and phase 2. These two phases could be, for example, a cracked porous rock, or a porous rock with different inclusions. Although the patchy saturation equations can be written with a very similar formalism, we do not here solve such problems. In simple terms, an internal fluid transfer mechanism (inner flow) is introduced to describe the flow between phase 1 and phase 2 in this theory. This provides an important energy dissipation mechanism for explaining the high attenuation at seismic frequencies, which cannot be explained by classic Biot theory applied to homogenous porous rocks. The original DPDP model can be reduced to an effective Biot model on the assumption that phase 2 is totally embedded in phase 1. It is also generally assumed that the included phase 2 is more compressible and has a higher porosity/permeability than the host phase 1. The inner flow mechanism is incorporated into the effective coefficients of the governing equations (here we refer to this DPDP model as the effective Biot theory). The phase velocity and attenuation dispersion characteristics of the *P* wave for the effective Biot theory are claimed to provide a good match with those measured in real rocks over the seismic frequency band (Pride *et al*. 2004).

Double porosity theory not only provides a more general model to describe the attenuation mechanism, but also the governing equations to calculate the averaged wavefields in porous media having mescoscopic heterogeneities. Otherwise, using just the original Biot theory, it is very difficult to numerically model a macroscopic wave in a porous medium (of dimensions hundreds to thousands of metres) having mescoscopic heterogeneities (with a size of several millimetres). However, it is not possible to analytically solve the field equations in heterogeneous double porosity media. This requires a numerical approach. Although there are several methods to numerically solve the wave equations, like the finite element method and the finite difference method (see the review article by Carcione *et al*. 2010), wave propagation in fluid-filled porous media presents special difficulties for modelling because of the interaction between the solid frame and the pore fluid. For example, the equations are

stiff and the moduli are frequency-dependent. This implies energy dissipation and the solutions should be expressed as convolution integrals in the time domain.

Poro-viscoelastic equations have been successfully solved by Carcione (2007) in the time domain to simulate Biot's (1962) energy dissipation model and the squirt-flow mechanism (Dvorkin *et al*. 1994) using a single Zener element at ultrasonic frequencies. However, Liu *et al*. (2009c) show that the DPDP model is very hard to fit by a single Zener element over a broad frequency range. Instead, they chose the relaxation function, which just approximates the dispersion behaviour of the double porosity model around the source centre frequency. The wave propagation can then be well described by the poro-viscoacoustic model with a single Zener element over the seismic frequency band. The primary attraction of using a Zener model is that it allows the convolution integral to be replaced by memory equations for which the field quantities need not be stored at every time step. However, this approximation allows only two Zener relaxation times to represent the very complex DPDP attenuation mechanism and thus reduce the difficulty.

Although Liu *et al*. (2010) suggested that a Kelvin-Voigt replacement element could be a better approximation than a Zener element at low frequency, their investigation showed that this is true only at frequencies of less than 50 Hz. Furthermore, the advantage is not very significant, and the Zener element can provides a much better approximation for frequencies in the range 50 Hz to several hundred Hertz. Liu *et al*. (2009c) numerically simulated elastic waves in heterogeneous DPDP media using a 2-D algorithm, which carries the implicit assumption of a line source. In this paper the modelling will now be extended to 2.5-D (point source).

Under the assumption that the medium is invariant in one direction (taken here as the *y*-axis direction) the 3-D wavefield for a point source can be efficiently obtained from the 2.5-D solution, which involves solving multiple 2-D equations (one for each wavenumber). Therefore, the 2.5-D solution has the advantage of a 3-D wavefield but is much more computationally efficient than the classical 3-D solution. For example, in frequency-domain modelling in elastic media, Zhou *et al*. (2011) report for a rather modest example computer memory requirements of 4 GB and 30 GB for 2.5-D versus 3-D modelling. The corresponding run times on an SGI Altix 30000 supercomputer were 7 hr and 40 hr, respectively.

Although several approaches for 2.5-D modelling have been applied for seismic wave simulation in single-phase media, the literature on 2.5-D modelling in porous media is, to the best of our knowledge, almost non-existent. The one exception is the paper by Lu *et al*. (2008) which used the boundary element method and considered a standard Biot porous medium. However, here we address the question of double porosity and attenuation and apply the time splitting method for the non-stiff parts, an explicit fourth-order Runge-Kutta method for the time integration and a Fourier pseudospectral staggered-grid method for handling the spatial derivative terms (Carcione 2007; Liu *et al*. 2009c).

2 THEORY AND METHOD

Based on the DPDP model (Pride & Berryman 2003a,b), the governing equations for the poro-viscoelastic model can be written as (Liu *et al*. 2009c)

$$\dot{\boldsymbol{\sigma}} + \dot{p}_c \mathbf{I} = \dot{\psi}_s(t) * \left[\boldsymbol{\nabla}\mathbf{v} + (\boldsymbol{\nabla}\mathbf{v})^{\mathrm{T}} - \frac{2}{3}\boldsymbol{\nabla}\cdot\mathbf{v}\mathbf{I} \right] \tag{1}$$

$$-\begin{bmatrix} \dot{p}_c(t) \\ \dot{p}_f(t) \end{bmatrix} = \begin{bmatrix} \dot{\psi}_{11}(t) & \dot{\psi}_{12}(t) \\ \dot{\psi}_{21}(t) & \dot{\psi}_{22}(t) \end{bmatrix} * \begin{bmatrix} \boldsymbol{\nabla}\cdot\mathbf{v}(t) \\ \boldsymbol{\nabla}\cdot\mathbf{q}(t) \end{bmatrix} \tag{2}$$

$$-\boldsymbol{\nabla} p_f = \rho_f \dot{\mathbf{v}} + m\,\dot{\mathbf{q}} + (\eta/\kappa_0^*)\mathbf{q} \tag{3}$$

$$\boldsymbol{\nabla}\cdot\boldsymbol{\sigma} = \rho\,\dot{\mathbf{v}} + \rho_f \dot{\mathbf{q}} \tag{4}$$

Here $\boldsymbol{\sigma}$ is the average stress tensor acting over the volume; $\mathbf{v}$ is the average particle velocity of the solid grains; $\psi_s(t)$ and $\psi_{mn}(t)$ are the relaxation functions of the *S* wave and the *P* wave, respectively, whose Fourier transforms are complex frequency-dependent moduli (see Liu *et al*. 2009c). It is worth noting that $\psi_{12}(t)$ is equal to $\psi_{21}(t)$ just for the case where the governing equations are derived under host field assumption (see Liu 2009a for details). The quantity p_c is the total confining pressure; p_f is the average fluid pressure; $\mathbf{q}$ is the macroscopic fluid flux, ρ and ρ_f are the bulk density and fluid density, respectively; κ_0^* is the effective static permeability of the double porosity composite; $m = T\rho_f/\phi$, where ϕ is the overall porosity, and T denotes the tortuosity. In this paper, we are considering the low frequency range of Biot theory, and hence the relaxation function ψ (referring to $\psi_s(t)$ or$\psi_{mn}(t)$) can be represented by the single Zener model as

$$\psi = \breve{\psi}\, H(t), \tag{5}$$

where $H(t)$ is the Heaviside (unit step) function, and

$$\breve{\psi} = \psi(t=\infty)\left[1 - \left(1 - \frac{\tau^\varepsilon}{\tau^\sigma}\right)\exp\left(-\frac{t}{\tau^\sigma}\right)\right]. \tag{6}$$

Here $\psi(t=\infty)$ refers to the value of the relaxation function at infinite time and corresponds to the static or zero frequency modulus of DPDP media (Carcione 2007; Morency & Tromp 2008; Pride & Berryman 2003a,b).

The new memory variables e_{sij}, e_{pc} and e_{pf} are defined as

$$e_{sij} = \partial_t \breve{\psi}_s(t) H(t) * [v_{i,j} + v_{j,i} - \delta_{ij} 2 v_{i,i}/3] \tag{7}$$

$$e_{pc} = \partial_t \breve{\psi}_{11}(t) H(t) * \boldsymbol{\nabla}\cdot\mathbf{v} + \partial_t \breve{\psi}_{12}(t) H(t) * \boldsymbol{\nabla}\cdot\mathbf{q} \tag{8}$$

$$e_{pf} = \partial_t \breve{\psi}_{21}(t) H(t) * \boldsymbol{\nabla}\cdot\mathbf{v} + \partial_t \breve{\psi}_{22}(t) H(t) * \boldsymbol{\nabla}\cdot\mathbf{q} \tag{9}$$

Here the memory variables e_{sij}, e_{pc} and e_{pf} correspond to the shear stress in eq. (1), the total confining pressure p_c and the average fluid pressure p_f in eq (2). Then the convolution integrals in eqs (1) and (2) can be replaced by the memory equations (given later as eqs 14–16).

The 2.5-D governing equations for poro-viscoelastic wave propagation are obtained by taking a Fourier transform in the strike or medium-invariant (*y*) direction over all of the field quantities in the 3-D governing equations. Although this operation is fairly standard in elastic media (Furumura & Takenaka 1996), the results are novel for porous media. They are given in the following equations, where the indices i and j takes on the values x, y, z. However, when the partial derivative is with respect to y, it should be replaced by ik_y. For example, $\tilde{p}_{f,y}$ is replaced by $ik_y\tilde{p}_f$.

$$\dot{\tilde{v}}_i = -\frac{m}{\rho_f^2 - \rho m}\tilde{\sigma}_{ij,j} - \frac{\rho_f}{\rho_f^2 - \rho m}\tilde{p}_{f,i} - \frac{\rho_f \eta}{\kappa_0^*\left(\rho_f^2 - \rho m\right)}\tilde{q}_i \tag{10}$$

$$\dot{\tilde{q}}_i = \frac{\rho_f}{\rho_f^2 - \rho m}\tilde{\sigma}_{ij,j} + \frac{\rho}{\rho_f^2 - \rho m}\tilde{p}_{f,i} + \frac{\rho \eta}{\kappa_0^*\left(\rho_f^2 - \rho m\right)}\tilde{q}_i \tag{11}$$

$$\dot{\tilde{p}}_f = -\psi_{21}(t=\infty)\frac{\tau_p^\varepsilon}{\tau_p^\sigma}\tilde{v}_{i,i} - \psi_{22}(t=\infty)\frac{\tau_p^\varepsilon}{\tau_p^\sigma}\tilde{q}_{i,i} - \tilde{e}_{pf} \tag{12}$$

$$\left.\begin{aligned}\dot{\tilde{\sigma}}_{ij} = {} & \delta_{ij}\psi_{11}(t=\infty)\frac{\tau_p^\varepsilon}{\tau_p^\sigma}\tilde{v}_{i,i} \\ & + \psi_s(t=\infty)\frac{\tau_p^\varepsilon}{\tau_p^\sigma}\left[\tilde{v}_{i,j} + \tilde{v}_{j,i} - \delta_{ij}\frac{2}{3}\tilde{v}_{i,i}\right] \\ & + \delta_{ij}\psi_{12}(t=\infty)\frac{\tau_p^\varepsilon}{\tau_p^\sigma}\tilde{q}_{i,i} + \delta_{ij}\tilde{e}_{pc} + \tilde{e}_{sij}\end{aligned}\right\} \tag{13}$$

$$\dot{\tilde{e}}_{sij} = \frac{\psi_s(t=\infty)}{\tau_s^\sigma}\left(1 - \frac{\tau_s^\varepsilon}{\tau_s^\sigma}\right)\left[\tilde{v}_{i,j} + \tilde{v}_{j,i} - \delta_{ij}\frac{2}{3}\tilde{v}_{i,i}\right] - \frac{1}{\tau_s^\sigma}\tilde{e}_{sij} \tag{14}$$

$$\dot{\tilde{e}}_{pc} = \frac{1}{\tau_p^\sigma}\left(1 - \frac{\tau_p^\varepsilon}{\tau_p^\sigma}\right)[\psi_{11}(t=\infty)v_{i,i} + \psi_{12}(t=\infty)q_{i,i}] - \frac{1}{\tau_p^\sigma}\tilde{e}_{pc} \tag{15}$$

$$\dot{\tilde{e}}_{pf} = \frac{1}{\tau_p^\sigma}\left(1 - \frac{\tau_p^\varepsilon}{\tau_p^\sigma}\right)[\psi_{21}(t=\infty)v_{i,i} + \psi_{22}(t=\infty)q_{i,i}] - \frac{1}{\tau_p^\sigma}\tilde{e}_{pf} \tag{16}$$

The tilde symbol above the field quantities in the above equations stands for Fourier transformation with respect to the y-coordinate. The quantity δ_{ij} is the Kronecker delta; $\tau_{p,s}^{\sigma,\varepsilon}$ are the Zener relaxation times which can be calculated from the dissipation factor $Q_p(f)$ of the DPDP model at the source centre frequency f (Liu *et al*. 2009c), but there is no existing model to calculate $Q_s(f)$ in spite of several investigations on shear attenuation by scattering (Masson & Pride 2007; Liu *et al*. 2009b). It was shown by Pride (2005) that in the case of spherical inclusions, the quality factor $Q_s(f)$ is the same for both the double porosity medium and the single porosity medium, and that this corresponds to the highest limit for $Q_s(f)$. Liu *et al*. (2009b) developed a solution for *S*-wave scattering by spherical poroelastic obstacles in a dissimilar poroelastic host rock and found that the internal fluid flow between the two phases does not cause much attenuation (unlike the compressional wave case). Here in this paper, we set $Q_s(f)$ equal to$Q_p(f)$ for the sake of simplicity. Adding a source vector **S**, the 2.5-D governing eq. (10) through (16) can be rewritten in matrix form as

$$\dot{\tilde{\mathbf{F}}} = \tilde{\mathbf{M}}(k_y)\tilde{\mathbf{F}} + \mathbf{S}, \tag{17}$$

where the quantity $\tilde{\mathbf{M}}(k_y)$ is the propagation matrix; $\tilde{\mathbf{F}}$ is the field vector to be solved for, given by

$$\begin{aligned}\tilde{\mathbf{F}} = [&\tilde{v}_x, \tilde{v}_y, \tilde{v}_z, \tilde{q}_x, \tilde{q}_y, \tilde{q}_z, \tilde{\sigma}_{xx}, \tilde{\sigma}_{yy}, \tilde{\sigma}_{zz}, \tilde{\sigma}_{xy}, \tilde{\sigma}_{yz}, \\ &\tilde{\sigma}_{xz}, \tilde{p}_f, \tilde{e}_{pc}, \tilde{e}_{pf}, \tilde{e}_{sxy}, \tilde{e}_{syz}, \tilde{e}_{sxz}]\end{aligned} \tag{18}$$

and the quantity **S** is the source vector which is located at $(x_0, 0, z_0)$ and written as

$$\begin{aligned}\mathbf{S} = [&0,\ 0,\ 0,\ 0,\ 0,\ 0,\ s_{xx},\ s_{yy},\ s_{zz},\ s_{xy},\ s_{yz},\ s_{xz}, \\ &s_f,\ 0,\ 0,\ 0,\ 0,\ 0]\delta(x - x_0)\delta(z - z_0).\end{aligned} \tag{19}$$

The pseudo-spectral staggered-grid method and the time-splitting method (for the stiff equations, see Carcione 2007) are applied to solve these simultaneous first-order equations. Since the terms involving $\rho_f\eta/(\kappa_0^*(\rho_f^2 - \rho m))$ $(i = x, y, z)$ in eqs (10) and (11) cause the 2.5-D governing equations to be stiff, they can be split into stiff parts and non-stiff parts. The stiff equations are

$$\dot{\tilde{v}}_i = -\frac{\rho_f\eta}{\kappa_0^*\left(\rho_f^2 - \rho m\right)}\tilde{q}_i \quad \text{and} \quad \dot{\tilde{q}}_i = \frac{\rho\eta}{\kappa_0^*\left(\rho_f^2 - \rho m\right)}\tilde{q}_i \tag{20}$$

These equations are solved analytically for every time step (Carcione 1995, 1996 and 2007) and the results are added to the results for every time step of the non-stiff equations. The non-stiff parts are solved using an explicit fourth-order Runge-Kutta method. The Fourier pseudo-spectral staggered-grid method is used to calculate the spatial derivatives (Carcione & Helle 1999). The reason for using a staggered grid is to reduce the numerical artefacts (Carcione & Helle 1999; ÖZdenvar & McMechan 1996).

Table 1. Staggered grid strategy

$\tilde{v}_x$	$(i+1/2, j, k)$	$\tilde{\sigma}_{xx}$	(i, j, k)	$\tilde{p}_f$	(i, j, k)
$\tilde{v}_y$	(i, j, k)	$\tilde{\sigma}_{yy}$	(i, j, k)	$\tilde{e}_v$	(i, j, k)
$\tilde{v}_z$	$(i, j, k+1/2)$	$\tilde{\sigma}_{zz}$	(i, j, k)	$\tilde{e}_q$	(i, j, k)
$\tilde{q}_x$	$(i+1/2, j, k)$	$\tilde{\sigma}_{xy}$	$(i+1/2, j, k)$	$\tilde{e}_{sxy}$	$(i+1/2, j, k)$
$\tilde{q}_y$	(i, j, k)	$\tilde{\sigma}_{yz}$	$(i, j, k+1/2)$	$\tilde{e}_{syz}$	$(i, j, k+1/2)$
$\tilde{q}_z$	$(i, j, k+1/2)$	$\tilde{\sigma}_{xz}$	$(i+1/2, j, k)$	$\tilde{e}_{sxz}$	$(i+1/2, j, k+1/2)$

The 2.5-D program code is simply extended from the 2-D code by solving a 2-D problem multiple times for each wavenumber k_y. Then, the 3-D wavefields are synthesized by applying an inverse Fourier transform in the k_y domain. The staggered grid points are illustrated in Table 1 in which the original grid is denoted by (i, j, k) and $i + 1/2$, $k + 1/2$ means the staggered derivatives.

It is worth noting that all the material parameters are unchanging along the *y*-axis, and therefore it does not make sense to define a staggered grid along the *y*-direction.

3 NUMERICAL EXAMPLES

To ensure numerical stability, the time integration requires that time step Δt and the largest eigenvalue $|\lambda_{\max}|$ satisfy the equation $\Delta t|\lambda_{\max}| < 2.78$ for the explicit fourth-order Runge-Kutta method, while the spatial derivative requires that the largest phase velocity $c_{\max}$ and grid spacing Δx satisfy the equation $c_{\max}\Delta t/\Delta x < 0.2$ for the Fourier pseudospectral method (see Carcione 2007). Here, the eigenvalues and phase velocities are calculated from the dispersion equation of the DPDP model (Liu *et al*. 2009c).

Three sample models were investigated. The models extend to 1280 m in the *x*–*z* plane and have a point source located at the point $x = 640$ m, $y = 0$ m and $z = 640$ m (z is in the downward direction). A staggered grid of 128 by 128 points is used in the *x*–*z* plane with a constant grid spacing of $\Delta x = \Delta z = 10$ m. The wavenumbers in the *y* direction are chosen as $2\pi n/(128\Delta x)$, where n ranges from 1 to 64. Note that for time-domain modelling, as opposed to frequency-domain 2.5-D modelling, there are no critical wavenumbers to consider at which the spectra can become singular (see discussion at end of Section 3.3). Furthermore, unlike frequency-domain modelling the wavefield does not become more oscillatory at increasing wavenumber (Zhou & Greenhalgh 2006), so a regular sampling strategy is acceptable. The maximum wavenumber we use, corresponding to $n = 64$ ($k_y^{\max} = 2\pi/(2\Delta x)$), is the Nyquist limit. The solid particle velocity waveforms v_z and the pore pressure waveforms p_f are recorded at the receiver positions (740, 100, 540), (840, 200, 440), (940, 300, 340), (1040, 400, 240) and (1140, 500, 140). In a spherical coordinate system having its centre at the source, the position coordinates of the receivers mentioned above are all along the direction having an inclination $\theta = -45^\circ$ and an azimuth $\varphi = 45^\circ$, but with increasing radii r of 173.2 m,

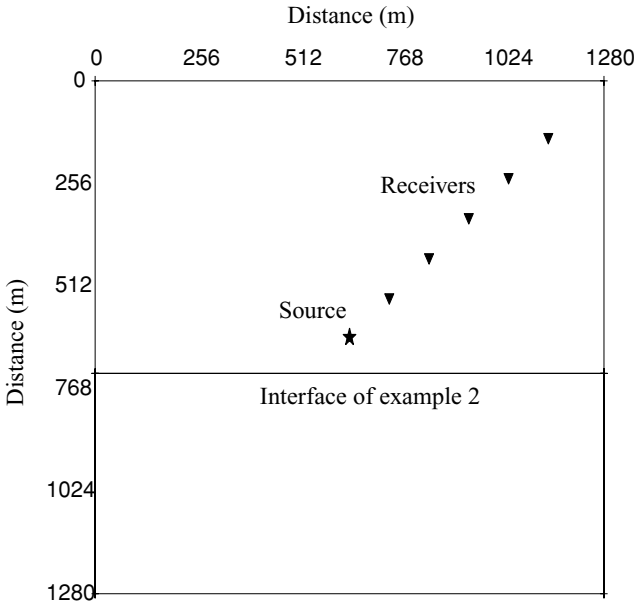

Figure 1. The 2.5-D model extends 1280 m in the horizontal (x) and vertical directions (z). The distances are shown along the x and z axes, with a grid spacing of 10 m. The source pulse has a centre frequency of 50 Hz and is located at (640 m, 640 m) and the five receivers are located at positions (740, 100, 540), (840, 200, 440), (940, 300, 340), (1040, 400, 240) and (1140, 500, 140). The source–receiver distances are 173.2 m, 346.4 m, 519.6 m, 692.8 m and 866.0 m, respectively.

346.4 m, 519.6 m, 692.8 m and 866.0 m, respectively. Fig. 1 shows the receiver configuration projected onto the x–z plane.

3.1 Model 1

The first model is a homogeneous material whose material properties are listed in Table 2 (see also table 1 of Liu *et al*. 2010), and for which we later set the volume fraction of the included phase 2 to zero to simulate a single porosity medium (a special case of the DPDP solid). This medium is the same as material B in the paper by Liu *et al*. (2009c) and corresponds to a 10 m deep sandstone layer with 3 per cent sand inclusions according to Walton theory and the Hashin and Shtrikman bound (see Pride *et al*. 2004 for details).

The source is taken to be a point force in the z-direction

$$\mathbf{S} = [0,\ 0,\ 0,\ 0,\ 0,\ 0,\ 0,\ 0,\ -1,\ 0,\ 0,\ 0,\ 0,\ 0,\ 0,\ 0,\ 0,\ 0]$$
$$\delta(x - x_0)\delta(z - z_0)h(t), \tag{21}$$

where the pulse $h(t)$ is a Ricker wavelet time function given by (Carcione 2007)

$$h(t) = \exp\left[-\frac{1}{2}\left(f_c^s\right)^2 (t - t_0)^2\right] \cos\left[\pi f_c^s (t - t_0)\right] \tag{22}$$

with $t_0 = 3/f_c^s$ and f_c^s is the source centre frequency.

The centre frequency of the Ricker wavelet source is chosen to be 50 Hz. The Biot characteristic frequency for this material is calculated from $\eta\beta/2\pi\rho_f T\kappa_0$ to be 4.1×10^4 Hz. It is much higher than our source centre frequency and so the low frequency requirement of eq. (3) is also satisfied. From Table 2 (see also table 2 of Liu *et al*. 2010—same material parameters), the acoustic specific quality factor Q_p of material B at a frequency of 50 Hz is 30, so the equivalent Q_p of the single Zener element at 50 Hz is also 30. The corresponding single Zener element is represented by a strain relaxation time and a stress relaxation time of $\tau^\varepsilon = 3.30 \times 10^{-3}$ and $\tau^\sigma = 3.07 \times 10^{-3}$, respectively (see Liu *et al*. 2009a,b,c, 2010).

To date the DPDP theory has only been developed for P waves, although Liu *et al*. (2009b) extended the treatment for the scattering of S waves by poroelastic obstacles in a poroelastic host. For the sake of simplicity, the same single Zener element is used to approximate the energy absorption of shear waves in the DPDP composite. Then, the shear modulus can be obtained from the following complex modulus of a Zener element given by Carcione (2007) as

$$M_z(\omega) = M_z^R \frac{1 - \mathrm{i}\omega\tau^\varepsilon}{1 - \mathrm{i}\omega\tau^\sigma}, \tag{23}$$

where M_z^R is the relaxed modulus.

To compare with our numerical result, we first compute the response of a single phase, homogeneous Biot medium. This is based

Table 2. Material properties of the sample rocks and fluids

Grain and fluid				
Parameter	Grains	Parameter	Water	
K_s(N m^{-2})	3.9×10^{10}	K_f(N m^{-2})	2.25×10^9	
G_s (N m^{-2})	4.41×10^{10}	ρ_f(kg m^{-3})	1000	
ρ_s(kg m^{-3})	2650.0	η_f(kg m^{-1} s^{-1})	0.001	
Material B (corresponding to 10 m deep double porosity sandstone)				
Parameter	Phase 1	Phase 2	Parameter	Composite
K_{dj}(N m^{-2})	2.23×10^{10}	2.04×10^8	K_d(N m^{-2})	7.85×10^9
G_{dj}(N m^{-2})	2.20×10^{10}	1.22×10^8	G_d(N m^{-2})	5.98×10^9
L1 (m)	0.0086	0.0086	ν_2	0.03
β_j	0.20	0.36	$c_p(50)$(ms^{-1})	2475
κ_{0j}(m^2)	1.0×10^{-14}	1.0×10^{-9}	$c_s(50)$(ms^{-1})	1608
Λ(m)	0.005		$Q_p(50)$, $Q_s(50)$	30.4

Composite relationships: porosity β $\beta = (1 - \nu_2)\beta_1 + \nu_2\beta_2$.
Permeability κ_0 $1/\kappa_0 = (1 - \nu_2)/\kappa_{01} + \nu_2/\kappa_{02}$.
Tortuosity T $T = \beta^{-2/3}$.

Notes: The physical meaning of the various parameters (Pride *et al*. 2004) is as follows: Subscript j denotes Phase 1 or 2; $K_{s,d,f}$ is bulk modulus of grain(s), drained porous frame (d) or fluid (f), respectively; $G_{s,d}$ shear modulus of grain and porous frame; $\rho_{s,f}$ density of grain or fluid; η_f viscosity; L1 is the characteristic length of the fluid pressure gradient; ν_2 volume fraction of phase 2; β porosity; κ_0 hydraulic permeability; Λ volume-to-surface ratio; T is tortuosity; $c_{p,s}(50)$ and $Q_{p,s}(50)$ are the phase velocity and quality factor for the fast P wave and the S wave at a frequency of 50 Hz, respectively.

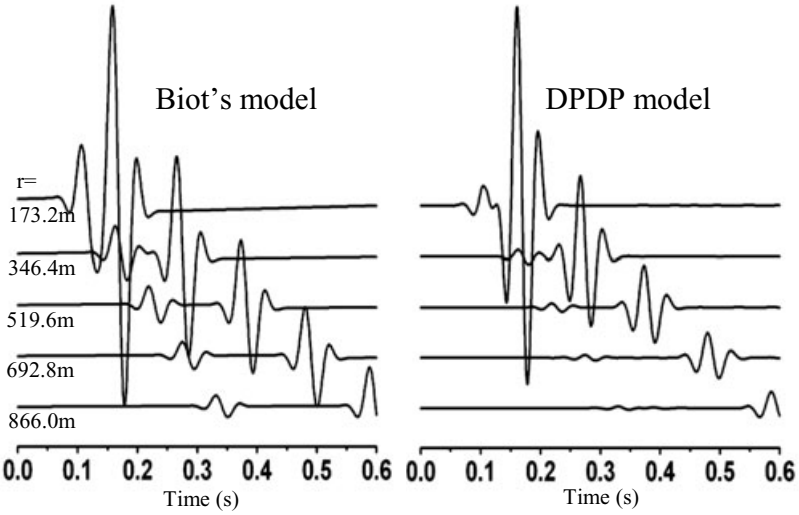

Figure 2. Waveforms of the normalized solid frame particle velocity of the z-component v_z in a homogeneous porous medium with a z-directed point force source. The receiver locations are along the polar angle of -45^0 and radii (r) of 173.2 m, 346.4 m, 519.6 m, 692.8 m and 866.0 m, respectively. Analytically calculated results based on Biot's theory (on the left hand side) are compared with the numerical simulation based on the DPDP model (with 3 per cent sand inclusions, $v_2 = 0.03$). Both sets of waveforms show the direct P wave and the direct S wave. The waveforms and amplitudes are different in each case comparable in each case.

on the analytic solution for the Green's function provided by Pride & Haartsen (1996). This same analytic solution was also applied by Karpfinger *et al*. (2009) to investigate the radiation patterns in poroelastic solids. The material properties are set to be the same as those of the host phase of the DPDP model (see Table 2). Since the point force is along the z direction, and the Greens function (Pride & Haartsen 1996) is formulated in spherical coordinates, we had to effect a coordinate transformation to use the analytical solution formulas. The details are given in the Appendix.

Seismograms were computed for five receivers at increasing radial distance from the source, in the range 173–866 m (see Fig. 1 for source–receiver geometry, but the model here is a full space of material forming the upper layer). Fig. 2 shows the normalized waveforms of the solid frame particle velocities of the z component, v_z. The analytical solution of Biot's model is plotted on the left hand side of the figure, whereas the numerical result for the homogensous DPDP model (with volume fraction of the included phase $v_2 = 0.03$) is plotted on the right hand side. Both images clearly show the P wave and the S wave. The S waves have much larger amplitudes than the P waves for the point source. Here, Biot's model and the DPDP model have almost the same group velocities for the P- and S-waves, but the amplitudes are different between the two cases, indicating different attenuation with distance from the source. To provide a closer look at such amplitude and waveform differences, we show in Fig. 3 a comparison of seismograms at a radius of 692.8 m. Both Figs 2 and 3 clearly show that the numerical solution for the double porosity medium gives lower amplitudes compared to the single porosity case (Biot analytic solution) because of higher attenuation associated with the double porosity inner flow mechanism.

In Fig. 4, we compare the analytical solution of Biot's model (on the left hand side) with our numerical result for the DPDP model (right hand side) but with only the host phase present ($v_2 = 0$). We find a strong similarity between the two models. However, the amplitudes of the P waves from our numerical solution are a little smaller than those of the analytic solution. We have checked our code and formulae but could not identify the reason for the small discrepancy. It is left as topic for future investigation.

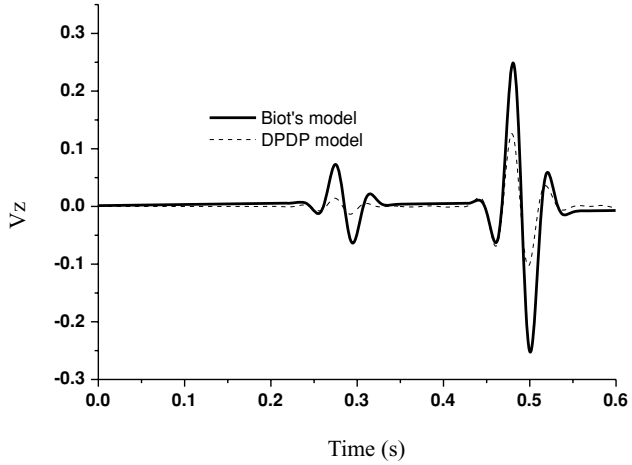

Figure 3. Waveforms of the normalized solid frame particle velocity for the z-component v_z in a homogeneous porous medium with the z-directed point force source. The receiver locations are along the polar angle of -45^0 and a radius (r) of 692.8 m. Analytically calculated results based on Biot's theory (solid line) are compared with the numerical simulation based on the true DPDP model (dashed line). The events in the DPDP model are more strongly attenuated.

3.2 Model 2

The second sample model involves two-dissimilar layers separated by a horizontal interface at a depth Z = 740 m (see Fig. 1). This sample model has a similar structure (interface and upper layer) to that used by Liu *et al*. (2009c). The difference is that Liu *et al*. (2009c) considered only 2-D modelling and used different model extents. The upper layer in model 2 is the DPDP material B, which is identical to that in model 1. The point force source is the same as that in the previous section for model 1. To obtain a strong reflection, the lower layer is chosen to be a Biot porous medium, which corresponds to phase 1 sandstone at a depth of 10 km according to Walton theory (see Pride *et al*. 2004 for details). The grain and fluid material properties are the same as the previous example, with the frame

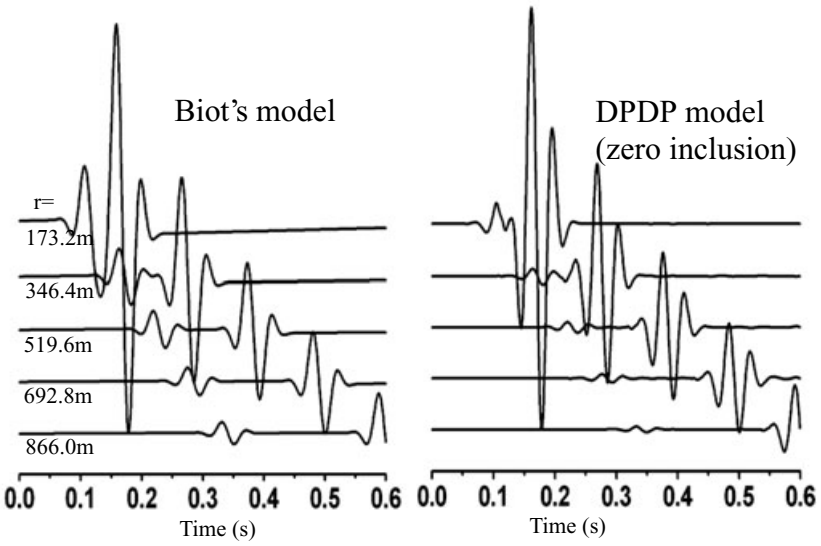

Figure 4. Waveforms of the normalized solid frame particle velocity of the z-component v_z in a homogeneous porous medium with a z-directed point force source. The receiver locations are along the polar angle of -45^0 and radii (r) of 173.2 m, 346.4 m, 519.6 m, 692.8 m and 866.0 m, respectively. Analytically calculated results based on Biot's theory (on the left hand side) are compared with the numerical simulation based on the DPDP model (but single phase with $v_2 = 0$). Both sets of waveforms show the direct P wave and the direct S wave. The amplitudes and waveforms are comparable in each case.

Table 3. Material properties of the lower layer rocks of Model 2 (see Fig. 1).

K_d(N m^{-2})	G_d(N m^{-2})	β	κ_0(m^2)
2.925×10^{10}	3.04×10^{10}	0.1	1.0×10^{-16}

properties now listed in Table 3. As a special case of the double porosity model, the volume fraction of phase 2 is set equal to zero in this lower layer. The single phase Biot porous medium does not have the internal flow mechanism and the relaxation frequency of the Biot viscodynamic mechanism is set at 1.0×10^8 Hz. So both materials can be well approximated by the poroelastic model (Liu *et al*. 2009c).

Fig. 5 shows the normalized waveforms for both the solid vertical component particle velocity v_z (left hand side diagram) and the pore pressure p_f (right hand side diagram). The amplitudes are normalized with respect to the maxima of v_z andp_f, respectively, recorded at a distance of 173.2 m. The v_z waveforms show the direct P wave, the reflected P wave, the direct S wave and the reflected S wave, which are denoted by the symbols P, rP, S and rS,

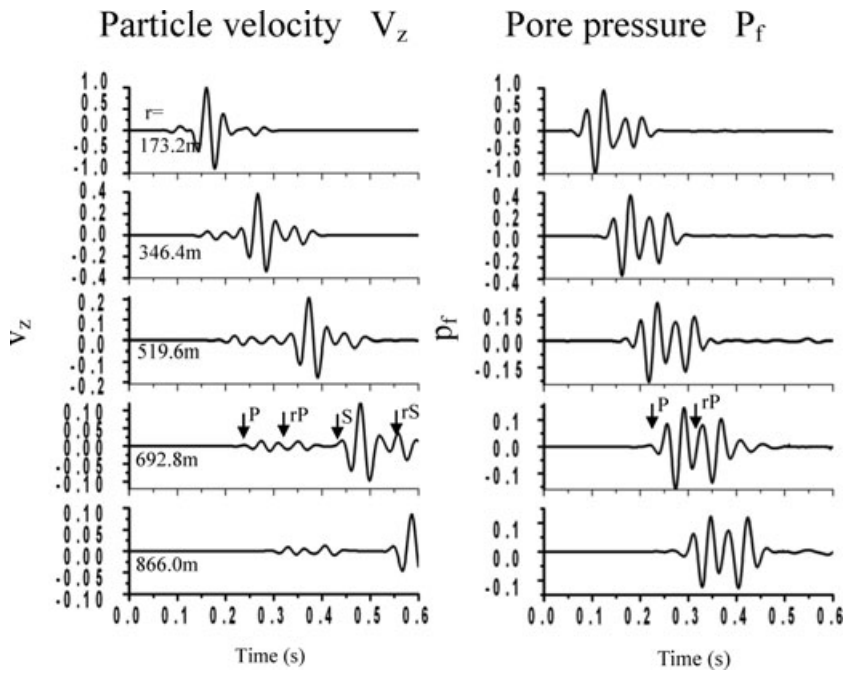

Figure 5. Waveforms of the normalized solid frame particle velocity of the z component v_z (on the left hand side) and the pore pressure p_f in a two-layer DPDP model. The source is a z-directed point force. The waveforms of v_z show the direct P wave, the reflected P-wave; the direct S-wave and the reflected S-wave, denoted as P, rP, S and rS, respectively. The waveforms of p_f (on the right hand side) show clearly the direct P-wave and the reflected P-wave, denoted as P and rP, respectively, but the shear wave events do not cause the pore pressure to change.

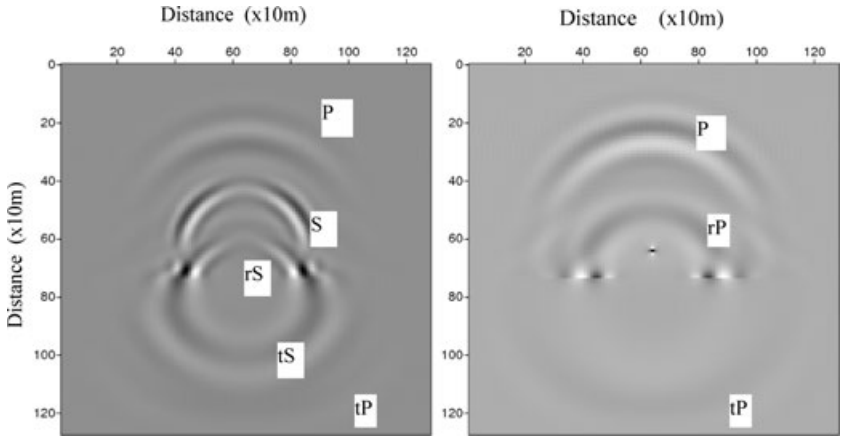

Figure 6. Snapshot of v_z (on the left hand side) and p_f (on the right hand side) at a time of 200 ms in a two-layer heterogeneous poro-viscoelastic medium. The distances are shown along the x and z axes, with a grid spacing of 10 m. The interface is at $z = 730$ m and the snapshots are in the x–z plane for $y = 10$ m. The source is point force and its pulse has a centre frequency of 50 Hz and is located at (640 m, 640 m).

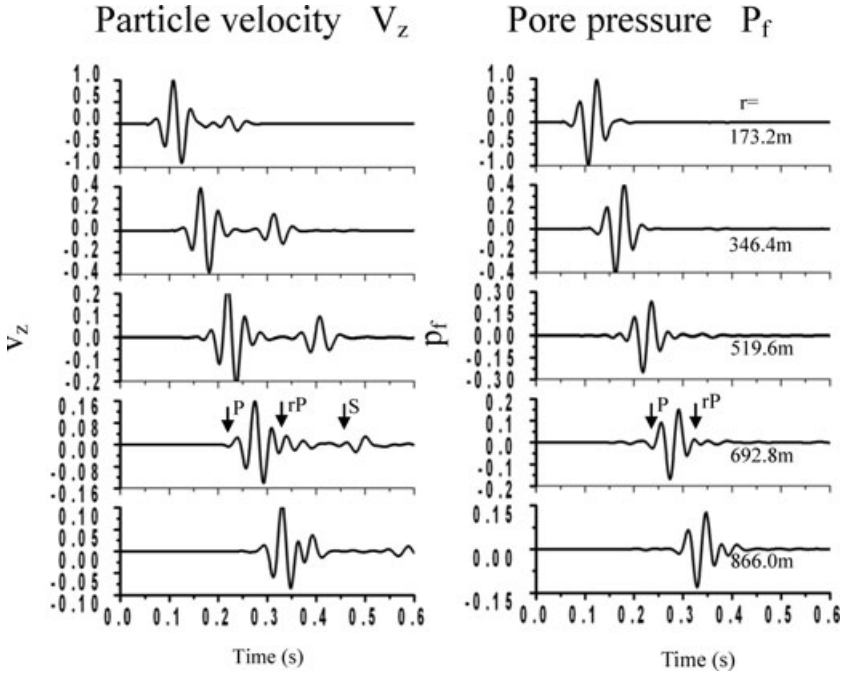

Figure 7. Waveforms of the normalized solid frame particle velocity of the z-component v_z (on the left hand side) and the pore pressure p_f in a two-layer DPDP model. The source is an explosion source. The waveforms of v_z show the direct P wave, the reflected P-wave; the mode-converted S-wave and denoted as P, rP, S respectively. The waveforms of p_f (on the right hand side) show clearly only the direct P wave and the reflected P wave.

respectively. The p_f waveforms clearly show the direct P-wave and the reflected P-wave, which are denoted by P and rP, respectively. In Fig. 6, we present wavefield snapshots in the x–z plane at a distance $y = 10$ m, at a time of 200 ms. The snapshot on the left is for the vertical particle velocity v_z and that on the right for fluid pressure p_f. The snapshots are in a plane very close to the central XOZ plane, so they are comparable to the snapshot for 2-D modelling given by Liu *et al*. (2009c). For v_z (on the left of Fig. 6), along the central vertical axis from top to the bottom, four clear wavefronts can be identified, corresponding to the direct P wave, the direct S wave, the reflected S wave and the transmitted S, denoted in the figure as P, S, rS, and tS, respectively. The transmitted P wave (denoted as tP, and almost off the edge of the plot) and the reflected P wave are not very clear due to interference. For p_f (on the right of Fig. 6), along the central vertical axis from top to the bottom, just three wavefronts are visible. They can be identified as the direct P wave, the reflected P wave and the transmitted P wave.

It should be remarked that the S waves (occurring in the v_z waveforms) do not change the pore pressure (right hand side waveforms) and therefore are not recognisable in the pressure plots of Figs 5 and 6. It is easy to understand that S waves do not cause any volumetric deformation and therefore do not significantly affect the pore pressure. However, some researchers discuss the existence of a slow S wave, which naturally arises when introducing a fluid strain-rate term in the Biot constitutive relation (see Sahay 2008 for details). But such a term is not included in our governing equation.

We next applied a volumetric (explosive) source, given by

$$\mathbf{S} = [0, 0, 0, 0, 0, 0, 1, 1, 1, 0, 0, 0, 1, 0, 0, 0, 0, 0] \times \delta(x - x_o)\delta(z - z_o)h(t) \tag{24}$$

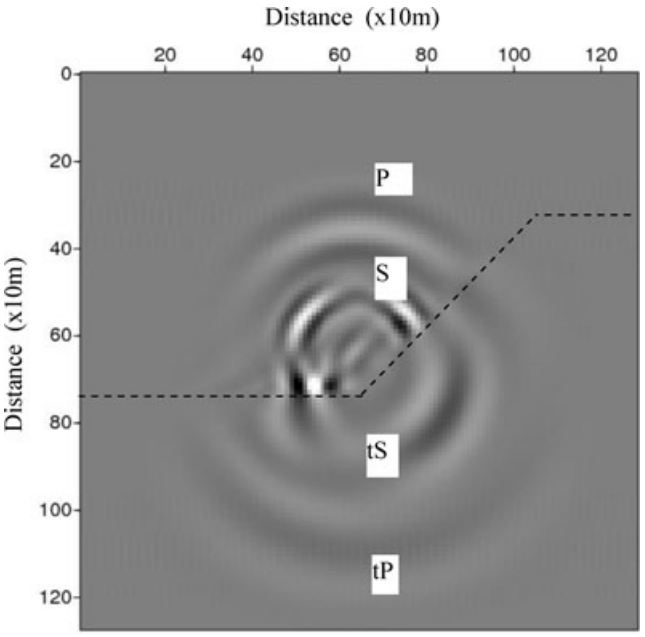

Figure 8. Snapshot of v_z at a time of 150 ms in a two-layer laterally varying poro-viscoelastic medium. The distances are shown along the x and z axes, with a grid spacing of 10 m. The interface is irregular and links the x and z coordinates (0, 740), (640, 740), (940, 440) and (1280, 440), showed as black dash line. The wavefield is in the x–z plane at $y = 10$ m. The source is point force and its pulse has a centre frequency of 50 Hz and is located at (640 m, 640 m).

and computed the particle velocity and fluid pressure waveforms for the same model and receiver geometry. The corresponding seismograms are shown in Fig. 7. The volumetric source produces only *P* waves. Again, we found that the shear wave event (a *P*-to-*S* mode converted reflection), recognizable in the particle velocity plot (left side waveforms), does not cause the pore pressure to change (right side waveforms).

3.3 Model 3

The third model has two-dissimilar layers comprising the same rocks as in model 2 but no longer separated by a horizontal interface. There is a clear lateral change (2-D model) compared to Fig. 1. Referring to this figure, the interface is located at a depth of 740 m between $x = 0$ and $x = 640$ m, then slopes upwards uniformly between $x = 640$ and $x = 940$ m, where it reaches a depth of 440 m (showed as black dashed line in Fig. 8). The interface then remains at this depth (horizontal) until $x = 1280$ m. Fig. 8 shows the wavefield snapshots for the vertical particle velocity v_z in the x–z plane of the model at a distance $y = 10$ m, and at a time of 150 ms. In this figure, along the central vertical axis from top to the bottom, four clear wavefronts can be identified, corresponding to the direct *P* wave, the direct *S* wave, the transmitted *P* wave and the transmitted *S*, denoted in the figure as *P*, *S*, *tS* and *tP*, respectively. The reflected *S* wave can be also identified in the central part of the figure, although its wavefront is much distorted by the irregular interface.

Finally, it is important to note that critical wavenumbers and singularity problems do not occur in our 2.5-D calculation scheme. It is well known (e.g. Zhou & Greenhalgh 2006) that, for perfectly elastic materials, the 2.5-D frequency-domain modelling method has a problem in both analytic and numerical solutions. Certain wavenumbers can cause spurious results and must be avoided in the wavenumber sampling strategy. The wavefield quantities theoretically become infinite at these so-called singular wavenumbers of k_y, which are referred to as critical values $k_y = \omega/c$, where c is the phase velocity of a particular wave. However, the poro-visoelastic wave approximation incorporates material attenuation, which essentially moves the poles off the real wavenumber axis along which the wavenumber spectra summation (inverse spatial Fourier transform) is performed.

CONCLUSIONS

For the double porosity Biot model, the local flow energy dissipation mechanism can be approximated by a single Zener viscoacoustic element. This replaces the convolution integrals of the governing equations with the memory equations for the memory variables which makes it unnecessary to store the field quantities at every time step. On the other hand, this approximation allows only two Zener relaxation times to represent the very complex DPDP attenuation mechanism and thus reduce the inversion difficulty. From the 3-D governing equations for poro-viscoelastic wave propagation, the 2.5-D governing equations are obtained by taking a Fourier transform in the medium-invariant (strike) y-direction and transforming to the wavenumber k_y domain. For heterogeneous, double porosity 2-D media, we obtain numerical 2.5-D transient solutions for a point source. This is accomplished by poro-visoelastic modelling using a time splitting method for the non-stiff parts and an explicit fourth-order Runge-Kutta method for the time integration and a Fourier pseudospectral staggered-grid for handling the spatial derivative terms. Since the 2.5-D scheme can be used to calculate the 3-D wavefields, it is clearly more realistic than 2-D (line source) modelling. By this method, the stress, particle velocity and pore pressure can be calculated simultaneously. We compare our numerical solution for the special case of a single porosity medium (setting $v_2 = 0$) with the analytical solution for a homogeneous Biot model and find there exists a slight discrepancy between the amplitudes of *P* waves, which requires further investigation. We have also presented results for heterogeneous (two layer) models, one incorporating lateral variations.

ACKNOWLEDGMENTS

We are grateful to the University of Adelaide, the Australian Research Council, ETH Zurich and the sponsors of the Centre for Reservoir Geophysics, Imperial College London, for supporting this research. We also thank two anonymous reviewers for their constructive suggestions, which have improved the quality of the paper.

REFERENCES

Biot, M.A., 1962. Mechanics of deformation and acoustic propagation in porous media, *J. Appl. Phys.,* **33**(4), 1482–1498.

Carcione, J.M., 1995. Some aspects of the physics and numerical modelling of Biot compressional waves, *J. Comput. Acoust.,* **3**(4), 261–280.

Carcione, J.M., 1996. Wave propagation in anisotropic, saturated porous media: plane-wave theory and numerical simulation, *J. Acoust. Soc. Am.,* **99**(5), 2655–2666.

Carcione, J.M., 2007. Wave fields in real media: wave propagation in anisotropic, anelastic, porous and electromagnetic media, in *Handbook of Geophysical Exploration, Seismic Exploration*, Vol. 38, 2nd edn, eds Helbig, K. & Treitel, S., Elsevier, Oxford.

Carcione, J.M. & Helle, H.B., 1999. Numerical solution of the poroviscoelastic wave equation on a staggered mesh, *J. Comput. Phys.,* **154**(2), 520–527.

Carcione, J.M., Morency, C. & Santos J.E., 2010. Computational poroelasticity – A review. *Geophysics,* **75**(5), 75A229–75A243.
Dvorkin, J., Nolen-Hoeksema R. & Nur A., 1994. The squirt-flow mechanism: macroscopic description, *Geophysics,* **59**(3), 428–438.
Furumura, T. & Takenaka, H., 1996. 2.5-D modeling of elastic waves using the pseudospectral method, *Geophys. J. Int.,* **124**, 820–832.
Karpfinger, F., Muller, T.M. & Gurevich, B., 2009. Green's functions and radiation patterns in poroelastic solids revisited, *Geophys. J. Int.,* **178**(1), 327–337.
Liu, X., 2009a. Seismic wave propagation and modelling in poro-elastic media with mesoscopic inhomogeneities. *PhD thesis*. The University of Adelaide.
Liu, X., Greenhalgh, S. & Zhou, B., 2009b. Scattering of plane transverse waves by spherical inclusions in a poroelastic medium, *Geophys. J. Int.,* **176**, 938–950.
Liu, X., Greenhalgh, S. & Zhou, B., 2009c. Transient solution for poro-viscoacoustic wave propagation in double porosity media and its limitations, *Geophys. J. Int.,* **178**, 375–395.
Liu, X., Greenhalgh, S. & Zhou, B., 2010. Approximating the wave moduli of double porosity media at low frequencies by a single Zener or Kelvin-Voigt element, *Geophys. J. Int.,* **181**, 391–398.
Lu, J.F., Jeng D.S. & Williams S., 2008. A 2.5D dynamic model for a saturated porous medium: Part II. Boundary element method, *Int. J. Solids Struct.,* **45**(2), 359–377.
Masson, Y.J. & Pride S.R., 2007. Poroelastic finite difference modeling of seismic attenuation and dispersion due to mesoscopic-scale heterogeneity, *J. geophys. Res.,* **112**, B03204, 1–16.
Morency, C. & Tromp, J., 2008. Spectral-element simulations of wave propagation in porous media, *Geophys. J. Int.,* **175**(1), 301–345.
Özdenvar, T. & McMechan, G.A., 1996. Causes and reduction of numerical artifacts in pseudo-spectral wavefield extrapolation, *Geophys. J. Int.,* **126**(3), 819–828.
Pride, S. 2005. Relationships between seismic and hydrological properties, in Hydrogeophysics, *Water Science and Technology Library*, pp. 253–284, Springer, Dordrecht.
Pride, S.R. & Berryman, J.G., 2003a. Linear dynamics of double-porosity and dual-permeability materials, I: governing equations and acoustic attenuation, *Phys. Rev. E*, **68**, 036603, 1–10.
Pride, S.R. & Berryman, J.G., 2003b. Linear dynamics of double-porosity and dual-permeability materials, II: fluid transport equations, *Phys. Rev.* E **68**, 036604, 1–10.
Pride, S.R., Berryman J.G. & Harris J.M., 2004. Seismic attenuation due to wave-induced flow, *J. geophys. Res.,* **109**, B01201, 1–19.
Pride, S.R. & Haartsen, M.W., 1996. Electroseismic wave properties, *J. acoust. Soc. Am.,* **100**(3), 1301–1315.
Sahay, P.N., 2008. Dynamic Green's function for homogeneous and isotropic porous media, *Geophys. J. Int.,* **147**(3), 622–629.
Zhou B. & Greenhalgh S.A., 2006, An adaptive wavenumber sampling strategy for 2.5D seismic-wave modeling in the frequency domain, *Pure appl. Geophys.,* **163**, 1399–1416.
Zhou, B., Greenhalgh, S.A. & Maurer, H., 2011. 2.5D frequency-domain seismic wave modelling in heterogeneous, anisotropic media using a Gaussian quadrature grid technique, *Comput. Geosci.*, in press.

APPENDIX: ANALYTICAL SOLUTION FOR SEISMIC WAVES IN A BIOT FLUID-FILLED POROUS MEDIA

The solid and the fluid relative displacement (**u**, **w**) caused by a body forces ($\mathbf{F}_s$, f_v) in a homogeneous and isotropic Biot porous medium are solved as (Pride & Haartsen 1996; Karpfinger *et al*. 2009):

$$\begin{pmatrix} \mathbf{u} \\ \mathbf{w} \end{pmatrix} = \begin{pmatrix} \mathbf{G}^{F,u} & \mathbf{G}^{f,u} \\ \mathbf{G}^{F,w} & \mathbf{G}^{f,w} \end{pmatrix} \cdot \begin{pmatrix} \mathbf{F}_s \\ f_v \end{pmatrix}. \tag{A1}$$

Here, the elements **G** are Green's tensors. For simplicity, we set the source at the centre of the coordinate system and the fluid volume source f_v to be zero, and we only calculate the solid displacement **u**. Thus, only $\mathbf{G}^{F,u}$ needs to be given here (for the other elements of the Green's tensor, please see Pride & Haartsen (1996) or Karpfinger *et al*. (2009). The calculation of **w** for non-zero f_v case can be obtained in the similar way.

$$\left.\begin{aligned} \mathbf{G}^{F,u}(\mathbf{r}) = \frac{1}{\mu}\frac{e^{i\omega S_3 r}}{4\pi r}(\mathbf{I}-\hat{\mathbf{r}}\hat{\mathbf{r}}) + \sum_{j=1}^{2} L^F_{u,S_j}\frac{e^{i\omega S_j r}}{4\pi r}\hat{\mathbf{r}}\hat{\mathbf{r}} + \\ \left[\begin{aligned} &\frac{1}{\mu}\left(\frac{i}{\omega S_3 r}-\frac{1}{(\omega S_3 r)^2}\right)\frac{e^{i\omega S_3 r}}{4\pi r} - \\ &\sum_{j=1}^{2} L^F_{u,S_j}\left(\frac{i}{\omega S_j r}-\frac{1}{(\omega S_j r)^2}\right)\frac{e^{i\omega S_j r}}{4\pi r} \end{aligned}\right](\mathbf{I}-3\hat{\mathbf{r}}\hat{\mathbf{r}}) \end{aligned}\right\}. \tag{A2}$$

and

$$\begin{aligned} L^F_{u,S_1} &= \left(\frac{M}{MH-C^2}\right)\left(\frac{S_1^2-\tilde{\rho}/M}{S_1^2-S_2^2}\right), L^F_{u,S_2} \\ &= \left(\frac{M}{MH-C^2}\right)\left(\frac{S_2^2-\tilde{\rho}/M}{S_2^2-S_1^2}\right). \end{aligned} \tag{A3}$$

(Noting the formalism of L^F_{u,S_1} in Karpfinger *et al*. 2009)

$$\left.\begin{aligned} 2S_1^2 &= \gamma - \sqrt{\gamma^2 - 4\tilde{\rho}\rho_t/(MH-C^2)} \\ 2S_2^2 &= \gamma + \sqrt{\gamma^2 - 4\tilde{\rho}\rho_t/(MH-C^2)} \\ S_3^2 &= \rho_t/\mu \quad \gamma = \frac{\rho M + \tilde{\rho}H - 2\rho_f C}{HM-C^2} \end{aligned}\right\}. \tag{A4}$$

Here S_1, S_2 and S_3 are the fast compressional, slow compressional and shear slowness, respectively.

$$C = \alpha M, \quad 1/M = (\alpha - \phi)/K_g + \phi/K_f, \quad H = K_{sat} + 4\mu/3 \tag{A5}$$

$$K_{sat} = K + \alpha^2 M, \quad \alpha = 1 - K/K_g, \tag{A6}$$

$$\rho_t = \rho - \rho_f^2/\tilde{\rho}, \quad \tilde{\rho}(\omega) = i\eta/(\omega\kappa(\omega)), \quad \rho = \phi\rho_f + (1-\phi)\rho_g \tag{A7}$$

$$\left.\begin{aligned} \kappa(\omega) &= \kappa_0 \Big/ \left(\sqrt{1 + i4\omega/(\omega_t m)} + i\omega/\omega_t\right) \\ \omega_t &= \eta\phi/(T_\infty \kappa_0 \rho_f) \quad 4 \le m \le 8 \end{aligned}\right\}. \tag{A8}$$

In the above K_f, K_g and K are the bulk moduli of the fluid, solid grain and dry skeleton, respectively; ϕ, κ_0 and T_∞ are porosity, permeability and tortuosity respectively; η is fluid viscosity; ρ_f and ρ_g are the density of fluid and solid grain, respectively.

The point source at the centre of the coordinate is written as

$$\mathbf{F}_s = (0, 0, \hat{\mathbf{z}})F(\omega). \tag{A9}$$

The solid displacement, by (A1) is

$$\mathbf{u} = \mathbf{G}^{F,u}(\mathbf{r}) \cdot \mathbf{F}_s \tag{A10}$$

Noting that the components of the Green's tensor (or Green dyadic) are shown in spherical coordinates, we apply the following equations to transform the vector from spherical coordinates $(A_r, A_\theta, A_\varphi)^T$ into cartesian coordinate $(A_x, A_y, A_z)^T$

$$\begin{pmatrix} A_x \\ A_y \\ A_z \end{pmatrix} = \begin{pmatrix} \sin\theta\cos\varphi & \cos\theta\cos\varphi & -\sin\varphi \\ \sin\theta\sin\varphi & \cos\theta\sin\varphi & \cos\varphi \\ \cos\theta & -\sin\theta & 0 \end{pmatrix} \begin{pmatrix} A_r \\ A_\theta \\ A_\varphi \end{pmatrix} \tag{A11}$$

Inserting (A2) and (A9) into (A10) and applying (A11), we have the results from the dot product of

$$\left.\begin{aligned} \hat{\mathbf{r}}\hat{\mathbf{r}} \cdot \mathbf{F}_s &= F(\omega)\cos\theta\hat{\mathbf{r}} \\ &= F(\omega)\frac{1}{2}(\sin 2\theta\cos\varphi\hat{\mathbf{x}} \quad \sin 2\theta\sin\varphi\hat{\mathbf{y}} \quad 2\cos^2\theta\hat{\mathbf{z}})^T \end{aligned}\right\} \tag{A12}$$

$$\left.\begin{aligned} (\mathbf{I} - \hat{\mathbf{r}}\hat{\mathbf{r}}) \cdot \mathbf{F}_s &= (\hat{\boldsymbol{\theta}}\hat{\boldsymbol{\theta}} + \hat{\boldsymbol{\varphi}}\hat{\boldsymbol{\varphi}}) \cdot \mathbf{F}_s = -F(\omega)\delta(\mathbf{r})\sin\theta\hat{\boldsymbol{\theta}} \\ &= -F(\omega)\frac{1}{2}(\sin 2\theta\cos\varphi\hat{\mathbf{x}} \quad \sin 2\theta\sin\varphi\hat{\mathbf{y}} \quad -2\sin^2\theta\hat{\mathbf{z}})^T \end{aligned}\right\} \tag{A13}$$

$$\left.\begin{aligned} (\mathbf{I} - 3\hat{\mathbf{r}}\hat{\mathbf{r}}) \cdot \mathbf{F}_s &= (\mathbf{I} - \hat{\mathbf{r}}\hat{\mathbf{r}}) \cdot \mathbf{F}_s - 2\hat{\mathbf{r}}\hat{\mathbf{r}} \cdot \mathbf{F}_s \\ &= -F(\omega)\left(\frac{3}{2}\sin 2\theta\cos\varphi\hat{\mathbf{x}} \quad \frac{3}{2}\sin 2\theta\sin\varphi\hat{\mathbf{y}} \quad (3\cos^2\theta - 1)\hat{\mathbf{z}}\right)^T \end{aligned}\right\} \tag{A14}$$

Then, the component of the solid displacement in the $\hat{\mathbf{z}}$ direction is

$$u_z(\omega) = \left\{ \begin{aligned} &\frac{1}{\mu}\frac{e^{i\omega S_3 r}}{4\pi r}\sin^2\theta + \sum_{j=1}^{2} L^F_{u,S_j}\frac{e^{i\omega S_j r}}{4\pi r}\cos^2\theta + \\ &\left[\frac{1}{\mu}\left(\frac{i}{\omega S_3 r} - \frac{1}{(\omega S_3 r)^2}\right)\frac{e^{i\omega S_3 r}}{4\pi r} - \right. \\ &\left.\sum_{j=1}^{2} L^F_{u,S_j}\left(\frac{i}{\omega S_j r} - \frac{1}{(\omega S_j r)^2}\right)\frac{e^{i\omega S_j r}}{4\pi r}\right]\left(1 - 3\cos^2\theta\right) \end{aligned} \right\} F(\omega). \tag{A15}$$

The particle velocity v_z is obtained by temporal differentiation, which in the frequency domain is simply multiplication by $-i\omega$ viz. $v_z(\omega) = -i\omega u_z(\omega)$. The waveform in the time domain is obtained by inverse Fourier transformation.

The other components of the solid displacement (or velocity) vector can be easily derived in a similar way.